Fillet Radius Impact of Rectangular Insulated Wires on PDIV for Turn-to-Turn Insulation of Inverter-Fed Motors

H. Naderiallaf, M. Degano, *Senior Member, IEEE*, C. Gerada, *Senior Member, IEEE*, and D. Gerada, *Senior Member, IEEE*

***Abstract*— This contribution elucidates the impact of the fillet radius, a geometric feature of rectangular insulated wires not commonly considered, on the partial discharge inception voltage (PDIV) in low-voltage machine turn-to-turn winding insulation. Initial PDIV tests involve edgewise-insulated wire samples with a reference fillet radius. These measurements are performed under constant conditions: 30°C temperature, 35% relative humidity, and atmospheric pressure (1000 mbar). These tests are carried out under AC 50 Hz excitations, following IEC 60034-18-41 guidelines for inverter-fed motor insulation system qualification. Subsequently, a probabilistic PDIV predictive model is developed based on Schumann's streamer inception criterion (SCSIC). This expanded model then analyses and forecasts the impact of the fillet radius on PDIV and its associated dispersion level, within the context of the 2-parameter Weibull distribution and the given environmental conditions. Furthermore, a novel method is presented to understand partial discharge (PD) phenomenology and its destructive potential in rectangular insulated wires with varying fillet radii. This approach employs SCSIC-derived streamer inception parameters (SIPs): critical field line length (CFLL), air effective ionization coefficient (α_{eff}), PD inception field (E_{inc}), and firing voltage (V_{firing}). The developed probabilistic predictive model enables the selection of an optimal fillet radius value, facilitating the creation of a reliable insulation system with maximum PDIV and minimal PD-related damage.**

***Index Terms*— Partial discharges, partial discharge inception voltage, inverter-fed machines, rectangular wire, fillet radius.**

NOMENCLATURE

B10	10th percentile
CFL	Critical field line
CFLL	Critical field line length
FEM	Finite element method
FLL	Field line length
FR	Fillet radius
K	Schumann constant
PD	Partial discharge
PDIV	Partial discharge inception voltage
SCSIC	Schumann's streamer inception criterion
SIP	Streamer inception parameter

I. INTRODUCTION

TRANSPORT ELECTRIFICATION has gained global attention as a means to decarbonize the transportation industry while improving air quality and reducing acoustic noise. Countries annually regulate CO_2 emissions from automobiles due to the escalating concern of global warming. Consequently, the automotive industry has advanced electric propulsion options, such as electric vehicles (EVs) and hybrid electric vehicles (HEVs), to effectively mitigate CO_2 emissions [1]. At the core of electric vehicles lies the drive system, composed of the battery, inverter, and traction motor. In electric and hybrid vehicles (EVs and HEVs), traction motor coil windings are increasingly employing rectangular insulated wires, such as edgewise wires or hairpin flat wires. This strategic selection elevates motor efficiency beyond the capabilities of randomly wound windings [2]. The implementation of rectangular wires further enhances filling factors, resulting in reduced copper losses and increased power densities [3]. Additionally, contemporary trends involve adopting inverters with elevated DC bus voltages (e.g., 600-1000 V) and high *dV/dt* in order to conserve energy and boost power density. However, this progression introduces substantial electrical stress on the insulation between winding turns, resulting in notable PD activity. From an electrical insulation perspective, rectangular insulated wires are often favoured over conventional round wires due to their thicker insulation, which contributes to a higher PDIV. When aiming for a PD-free design, where the voltage drop across turn-to-turn insulation must remain below the minimum PDIV [4], the structured placement of rectangular insulated wires in formed-wound windings markedly simplifies voltage management in comparison to random wound configurations. Fig. 1 shows common coil

This paper was submitted for review in August 2023. This work was supported by the Clean Sky 2 Joint Undertaking through the European Union's Horizon 2020 Research and Innovation Programme under Grant 807081. *(Corresponding author: Hadi Naderiallaf).*

Hadi Naderiallaf, Michele Degano, Chris Gerada, and David Gerada are with the Power Electronics and Machines and Control (PEMC) Research Group, the University of Nottingham, Nottingham, U.K.
(e-mail: Hadi.Naderiallaf@nottingham.ac.uk; Michele.Degano@nottingham.ac.uk; Chris.Gerada@nottingham.ac.uk; David.Gerada@nottingham.ac.uk)

windings produced using edgewise-insulated wires.

Fig 1. Illustration of coil windings manufactured using edgewise-insulated wires.

The highest electrical stress, induced by PD activity, arises in the turn-to-turn insulation due to interactions between power converters and coil windings. Within the electrical machine insulation system, turn-to-turn insulation is the critical and vulnerable component for both randomly and formed-wound windings. Despite the heightened reliability and lifetime of phase-to-ground and phase-to-phase insulation systems in formed-wound windings, the turn-to-turn insulation system remains the most susceptible [5]. PD emerges as the foremost stress factor confronting turn-to-turn insulation. This becomes especially critical as the electric field linked to this insulation surpasses the PD inception field, prompting the onset of PD activity and accelerating insulation deterioration. This concern amplifies when winding wires are shielded solely by organic insulation, where PD can lead to premature failure, possibly reducing lifetime to days or hours [6]. Consequently, in the context of formed-wound winding technology, addressing PD becomes imperative throughout electrical machine insulation design, winding insulated wire selection, and manufacturing processes. To this end, three key considerations emerge. Firstly, a PD-free criterion must guide the design of inverter-fed machines using Type I insulation (comprising organic-only insulating materials) [4]. Secondly, meticulous selection and manufacturing of winding's wire insulation properties and geometry must maximize the PDIV, recognizing the constraints posed by maintaining insulation thickness without compromising the desired fill factor and power density. Thirdly, for manufacturing coil windings using rectangular insulated wires (Fig. 1), selecting an optimal bending radius is vital to improve insulation performance [7].

Insulation designers for electrical machines and manufacturers of winding insulated wires can significantly benefit from tools that facilitate the prediction of the effects of wire insulation material properties and geometry on PDIV. This obviates the necessity of constructing and testing representative insulation models, which can be both time-consuming and expensive. A strategy to predict PDIV involves Schumann's streamer inception criterion (SCSIC), which relies on the Schumann constant, K. This constant, a logarithmic representation of the critical electron count that demarcates the shift from Townsend to streamer discharge, was introduced in [8]-[13] to forecast PDIV within turn-to-turn insulation. This method explores how material properties (e.g., permittivity, insulation thickness), as shown in [8]-[10], and environmental conditions, as investigated in [11]-[13], affect PDIV. Yet, an unaddressed research gap persists: the absence of literature dealing with the modelling and analysis of the impact of the fillet radius (*FR*) of rectangular insulated wires on PDIV and the harmfulness associated with PD activity for turn-to-turn insulation. Regrettably, the pivotal role played by this geometric aspect of rectangular wires in determining PDIV has been disregarded. The existing research gap has led to the undervaluation of the effects of *FR*, which in turn leads to confusion when ordering or manufacturing rectangular wires. Electric machine designers, when working on the fill factor calculation, prioritize minimizing *FR* in insulated wires of rectangular shape, aiming at achieving maximum fill factor and simplifying calculations. Moreover, the non-sharp edges found in these wires are often attributed wrongly to inherent manufacturing limitations, sometimes overlooking the *FR* impact on PDIV. Conversely, there may be an awareness that sharp edges could mitigate PDIV, prompting wire manufacturers to consider maximizing *FR*. However, this is frequently done without identifying an optimal threshold for *FR* beyond which PDIV no longer increases. Furthermore, it is advantageous to recognize that while two distinct fillet radii might deliver a comparable PDIV, the damage resulting from PD activity at the same overvoltage with respect to PDIV for these radii might not be the same.

This contribution aims to fill the research gap by employing the SCSIC through FEM electrostatic simulations and ionization swarm parameter calculations. Initially, the goal is to quantitatively investigate how the *FR* of rectangular insulated wires affects the PDIV of turn-to-turn insulation. Subsequently, the study delves into the impact of this geometric feature on SCSIC-derived SIPs, including critical field line length (CFLL), PD inception field (E_{inc}), effective ionization coefficient (α_{eff}), and firing voltage (V_{firing}). These investigations not only enhance comprehension of PD phenomena concerning *FR* but also shed light on corresponding damage from PD activity. Based on these findings, an optimal *FR* for rectangular insulated wires in formed-wound windings can be determined—prioritizing maximum PDIV alongside minimal PD-associated damage. This contribution introduces another innovation by expanding the PDIV model proposed in [8]-[13]. This involves elevating the SCSIC to a probabilistic predictive model that reflects the true stochastic nature of PD. The approach introduces a probabilistic predictive model, using derived K values from varying percentiles of PDIV to estimate PDIV with specified probabilities and address the PDIV dispersion level as a function of *FR*.

To attain these objectives, the approach involves (a) measuring PDIV for turn-to-turn specimens made from a reference rectangular wire with a specific *FR*. Subsequently, (b) electric field simulations and calculations of ionization swarm parameters are conducted on the samples across various PDIV percentiles. (c) The SCSIC is then used to determine N_{c}, the threshold electron count representing the shift to streamer discharge. Additionally, (d) deriving K as the natural logarithm of N_{c}, is executed with diverse probabilities. As the fitting parameter, K remains unaffected by material properties and wire geometry within a given insulation type

(e.g., turn-to-turn using round or flat conductors) [9], (e) the derived K percentiles are maintained while only the FR varied. The obtained probabilistic K values are used to predict PDIV with different probabilities while the PDIV dispersion level in relation to the FR of rectangular insulated wires is derived. Finally, (f) the effect of the FR on SCSIC-derived SIPs is investigated using two distinct K values. The initial one, K_{B10}, represents a 10% probability within the 2-parameter Weibull distribution. The second, K_{mean}, is calculated from the mean PDIV values extracted from measurements. Employing these two different statistical K values facilitates the identification and validation of trends of SCSIC-derived SIPs as a function of FR.

II. Methodology

A. Test Samples

PDIV tests are conducted on sets of edgewise enamelled wires enclosed in polytetrafluoroethylene (PTFE), representing the insulation system found in turn-to-turn windings within electrical machines, as depicted in Fig. 2. The insulation of the wire consists of a polyester-imide base and a polyamide-imide topcoat, both conforming to a thermal classification of 200°C.

Fig. 2. Illustration of edgewise insulated wires shown both before (below) and after (top) being wrapped in PTFE, representing the test sample.

Fig. 3 presents the dimensions of the bare copper wire, insulation thicknesses on the flatwise, edgewise, and fillet sides, as well as the FR of the edgewise enamelled wire.

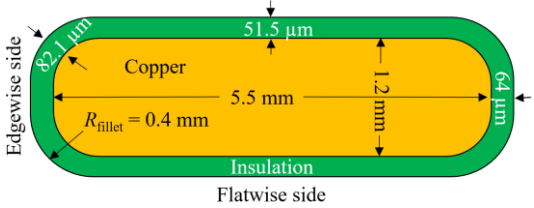

Fig. 3. Dimensions of the cross-section of edgewise insulated wire.

The cross-sectional dimensions of the wire, encompassing copper length and width, along with insulation thickness on both the flatwise and edgewise sides, are meticulously gauged using a micrometre screw accurate to 1 µm. The insulation thickness is ascertained by calculating the variation in dimensions before and after stripping. Wire stripping is conducted using a laser wire stripping device, assuring the removal of solely the insulation while preserving the copper. To acquire the necessary dimensions, 35 wires are subjected to measurement, and the averaged values are subsequently documented. Regarding the FR, it is specified as R_{fillet} = 0.4 mm by the wire manufacturer. Subsequently, the insulation thickness on the fillet side of the wires is determined through interpolation. This interpolation is accomplished using the sketch tools available in COMSOL, taking into consideration the measured insulation thicknesses on both the flat and edgewise sides. An additional crucial parameter for the FEM-based model is the relative permittivity, which plays a pivotal role in determining the electric field distribution within the electrostatic simulations. The relative permittivity of the enamel at the testing temperature of 30°C is measured to be 3.3. This measurement is carried out using a Megger Delta4000. Detailed information on the methodology used to measure the relative permittivity of the enamel can be found in [10].

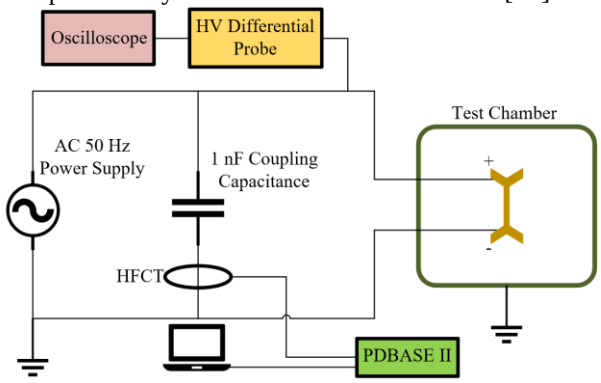

Fig. 4. Circuit layout and connection configuration for PDIV measurement setup.

B. PDIV Test Setup and Procedure

For evaluating turn-to-turn insulation in inverter-fed motors, IEC 60034-18-41 [4] offers the flexibility to measure PDIV under either sinusoidal or impulsive voltage excitations. AC 50 Hz supply yields a cautious evaluation of turn-to-turn insulation under 2-level inverter or surge generator waveforms [14]. It's important to note that the measured PDIV using AC 50 Hz excitation is generally lower than that obtained from steep-fronted square waveforms with rise times shorter than 1 µs [15]. It can be attributed to either or both of the following factors: (a) reduced permittivity due to the higher spectral frequency content of steep-fronted waveforms, or (b) the low probability of initiating PD when the rise time is fast [16]. As a result, AC PDIV tests are carried out under sinusoidal waveform excitation at 50 Hz in this study, ensuring that conservative PDIV values are obtained. The PDIV tests are conducted within a test chamber manufactured by Memmert. This controlled environment allows for precise regulation of temperature and humidity levels, enabling the tests to be carried out at a consistent temperature of 30°C, relative humidity (RH) of 35%, and atmospheric pressure (p) set at 1000 mbar.

In the PDIV test setup, the AC source employed is the GPT-9802 by GW Instek. The applied voltage across the specimen is continuously monitored using a Teledyne LeCroy WaveSurfer 510 oscilloscope featuring a bandwidth of 1 GHz and a sampling rate of 10 GS/s. This voltage is measured through a CT4079-NA differential probe characterized by a 50 MHz bandwidth, a 2000:1 voltage ratio, and a 50 Ω impedance. For PD detection, a conventional indirect circuit, outlined in Fig. 4, is implemented. To enhance the measurement sensitivity and

enhance the signal-to-noise ratio, a PD-free 1 nF coupling capacitor is connected in parallel with the test sample. The used PD sensor is a high-frequency current transformer (HFCT) with a ferrite core, designed by Techimp and offering a bandwidth spanning 1 to 60 MHz. The PD signals are detected by the Techimp PD BaseII detector, which features an acquisition frequency range extending from 16 kHz to 48 MHz, accompanied by a sampling rate of 200 MSa/s.

The PDIV test procedure commences with an initial voltage level that remains well below the PDIV threshold. Systematically, the peak of the applied voltage escalates incrementally by 10 V, with each step spanning 30 seconds. Upon the detection of PD, the peak voltage value at that moment is meticulously recorded as the PDIV. Conducting the PDIV measurements involves using five distinct test specimens, all of which remain previously unused. PDIV measurements are conducted once on each pristine specimen to prevent reduced accuracy stemming from residual charges from prior PD activities [17]. This approach also considers the potential PDIV reduction caused by insulation damage resulting from PD activity, especially given the organic nature of the insulation material. Consequently, five pristine samples are assessed to form a dataset for analysis. To conclude, the acquired experimental data is subjected to fitting with the 2-parameter Weibull distribution to determine the PDIV percentiles.

III. Stochastic SCSIC Development

The central aspect of the streamer inception criterion lies in the single-electron-avalanche mechanism. It is generally postulated that once the number of electrons at the head of the avalanche reaches a critical number of N_c, fast-moving filamentary streamers emanate from the avalanche's head, leading to the transition from Townsend to streamer discharge [18]. N_c is introduced through an exponential function linked to the Schumann constant, K, as (1) [19]:

$$N_c = exp\,(K) \tag{1}$$

Based on SCSIC [19], a Townsend avalanche undergoes the transformation into a streamer when condition (2) is met:

$$K \leq \int_0^{x_c} \alpha_{\text{eff}}(x) \cdot dx \tag{2}$$

where K is the natural logarithm of N_c, a dimensionless constant. Additionally, x denotes the distance passed by a single primary electron from the cathode where the avalanche begins, while x_c is the critical avalanche length along the electric field line beyond which the transition from Townsend to streamer discharge occurs, signifying the earliest discharge event. Moreover, α_{eff} represents the gas effective ionization coefficient, derived from (3):

$$\alpha_{\text{eff}} = \alpha_{\text{gas}} - \eta_{\text{gas}} \tag{3}$$

where α_{gas} and η_{gas} are gas ionization and the attachment coefficients, respectively, depending upon the gas type, electric field intensity, gas number density or its pressure, temperature, and humidity [20].

PDIV measurements are conducted once on each non-electrically stressed specimen for two primary reasons: (a) to prevent any potential reduction in PDIV caused by residual charges from prior PD activities, and (b) to account for the organic composition of the wire insulation (polyamide-imide), thereby averting the potential decrease in PDIV due to insulation damage resulting from PD activity [10], [11], [12], and [13]. In addition, to mitigate the potential influence of space charge accumulation on both the electric field distribution within the air wedge and the PDIV readings, it is recommended to employ bipolar excitations featuring polarity reversals (e.g., AC). This approach is favoured instead of using voltage waveforms that include a DC component (e.g., unipolar excitations) [16], [21], [22].

A. Electric Field Simulation between Wires with Different Fillet Radii

The non-uniform electric field distributions in the air wedge between two rectangular insulated wires, featuring nine different fillet radii, are simulated based on FEM using the electrostatics interface of the AC/DC module of COMSOL Multiphysics® software. The two-dimensional (2D) model is used to compute the electrostatic simulations. Table I reports the wire's cross-section dimensions (insulation thickness, bare copper dimensions, and *FR*) and relative permittivity (ε_r) which comprise the input parameters for the electrostatics interface.

TABLE I
WIRE'S CROSS-SECTION DIMENSIONS AND RELATIVE PERMITTIVITY

R_{fillet} (mm)	Insulation thickness (μm)			Copper width (μm)	Copper length (μm)	ε_r
	Flatwise side	Edgewise side	Fillet side			
0.4	51.5	64	82.1	1.2	5.5	3.3

These parameters are measured using the methodology detailed in Section II. Considering the 2D wire's cross-section geometry, the *FR* is the only variable that varies, ranging from 0.05 mm to 0.52 mm. The initial electrostatic simulations are performed with a unit voltage (i.e., 1V), [8]-[13], for every *FR* under consideration. These simulations yield reference databases that correspond to each specific *FR*.

The simulation output corresponding to each *FR* referred to as the reference database, comprises two essential components: 1) The list of FLLs exclusively located in the air wedge between the wires. These FLLs are sorted in ascending order based on their lengths, ranging from the shortest to the longest. 2) The corresponding electric field strengths associated with each FLL, consequently, featuring a decreasing trend. After conducting electrostatic simulations using COMSOL software, the lengths of field lines, which exclusively extend through the air, are computed, and illustrated in Streamline plots, forming part of the 2D plot group. These results are then exported to MATLAB for further analysis [10]-[13]. It is crucial to highlight that the electric field strengths are the ones that increase with higher

applied voltages, and these values are recalculated for each voltage level to keep the reference database up to date. However, the first component, i.e., the list of FLLs, remains constant and does not change with the increase in voltage levels.

The optimal number of electric field lines in the air wedge is chosen to maintain a distance not exceeding 1 μm between lines. This quantity varies with fillet radius, depending on conductor diameter and insulation thickness at the fillet side. The determination employs a function outlined in [12], with FEM simulations employing an extremely fine mesh size in this study. Further details on field line number determination were provided in [12].

Fig 5 illustrates the simulated electric field distribution between two edgewise insulated wires, showcasing two distinct fillet radii as examples: (a) R_{fillet} = 0.2 mm and (b) R_{fillet} = 0.52 mm. Fig. 5 illustrates, under a constant applied voltage, an increase in R_{fillet} enhances the range of electric field intensity variations between two rectangular wires. This can be attributed to the larger range of FLLs that the air wedge can accommodate when R_{fillet} is larger.

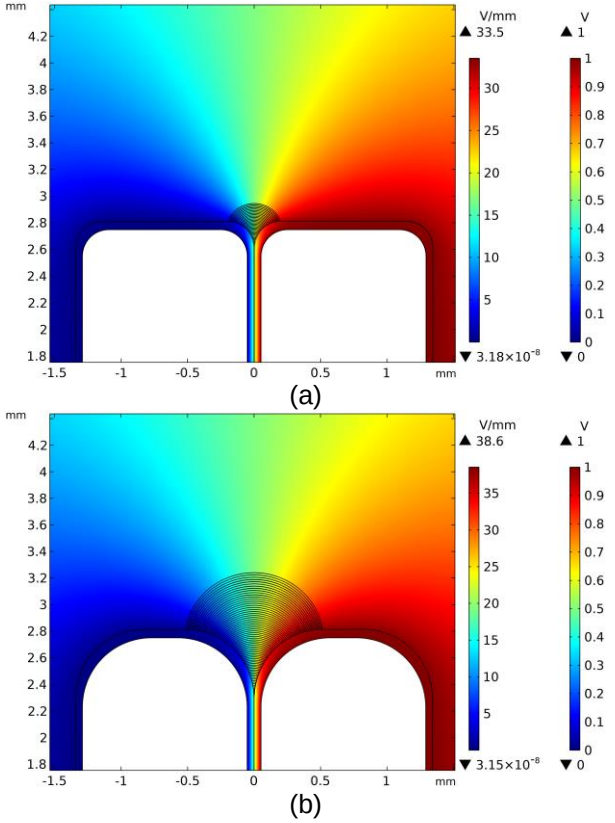

Fig. 5. Simulation of electric field distribution between two edgewise insulated wires using 2D COMSOL Multiphysics® with varying fillet radii, representing two examples (a) R_{fillet} = 0.2 mm and (b) R_{fillet} = 0.52 mm.

B. Air Effective Ionization Coefficient Calculation

The right-hand term in (2) should be computed along the length of each field line generated by FEM. To achieve this, it is imperative to determine the effective ionization coefficient of air (α_{eff}) along each field line, specifically where the discharge event occurs, using (3). This involves obtaining the gas ionization (α_{gas}) and attachment (η_{gas}) coefficients, which can be derived using BOLSIG+ software. The approach detailed in [10]-[13], is summarized succinctly as follows:

(a) Load ionization swarm parameters for dry air from the LXCAT database into the software [23], [24].

(b) Determine the composition of moist air as a percentage (%) under the specified test conditions (T=30°C, RH=35%, p=1000 mbar) and input these values into the software [10]-[13].

(c) Set the gas temperature in Kelvin within the software.

(d) Calculate and input the range limit of the reduced electric field, corresponding to the longest and shortest field lines in Townsend, into the software. The detailed methodology can be found in [10]-[13].

C. Deriving K from Different PDIV Percentiles

The algorithm described in [10]-[13] is implemented in MATLAB and developed to determine the K value from various PDIV percentiles. To obtain these PDIV percentiles, experimental data from the reference rectangular wire with R_{fillet} = 0.4 mm is fitted to the Weibull distribution. The step-by-step K calculation procedure is as follows:

1) The first step involves importing the reference database obtained from FEM electrostatic computations simulated with a unit voltage (i.e., 1 V), which includes the FLLs as a function of the electric field intensity.

2) In the second step, the electric field magnitude across each field line obtained in step 1 is updated by employing linearity through (4) considering the effect of PDIV. As PDIV is a stochastic variable, it is essential to treat PDIV in (4) as a statistic derived from the measured experimental PDIV values. Thus, (4) can be applied to various statistics of PDIV, such as the mean value, median, or other percentiles of the Weibull distribution fitted to the measured PDIV values as shown in Fig. 6.

$$E(x,y) = PDIV \cdot E_{\text{database}}(x.y) \quad (4)$$

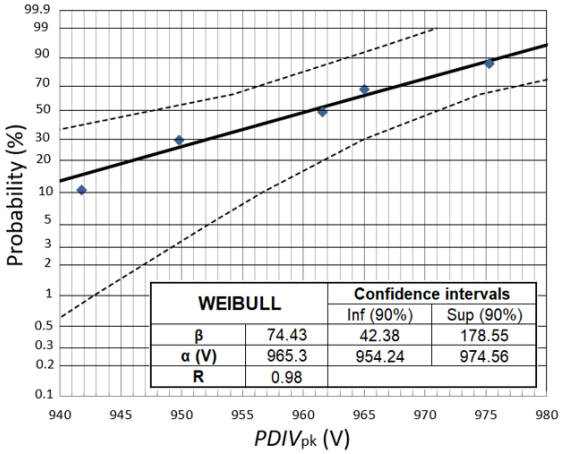

Fig 6. 2-parameter Weibull distribution fitted to the measured peak value of PDIV. The scale parameter (α), shape parameter (β) and correlation coefficient R are reported in the label.

3) In the third step, α_{eff} is calculated as a function of electric field intensity across each field line obtained in step 2 using the BOLSIG+ software [23], [24].
4) The next step involves computing the right term in (2) for all the field lines present in the air wedge formed between the two rectangular wires.
5) Finally, for different PDIV percentiles applied in (4), record the maximum value obtained in step 4. This maximum value is considered as the derived K associated with the selected PDIV percentile, which is then used in the SCSIC to predict PDIV with the required probability. For more clarification of the used approach, Fig. 7 provides an illustrative example of the procedure to determine K_{B10}, representing the K value obtained under the B10 of PDIV. Additionally, record the field line along which the maximum value of K is obtained as CFL, and report the length of the field line as CFLL [10]-[13].

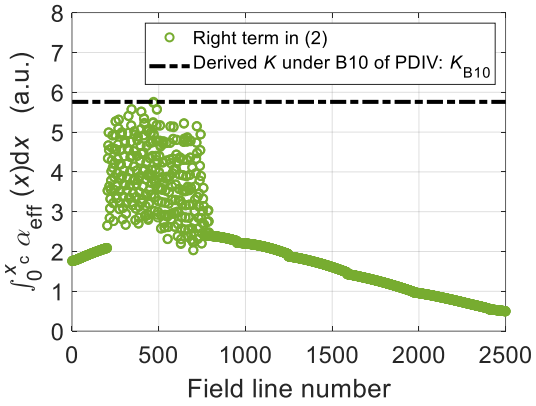

Fig 7. Visualizing the K determination method for PDIV estimation using SCSIC.

Fig. 7 reveals a critical region concerning the field line number, which significantly impacts α_{eff} and subsequently, the right term in (2), leading to a substantial increase [10]-[13]. Consequently, the maximum values of the right term in (2), thus K, are consistently located within this crucial region. This critical zone decisively determines K, and subsequently, it plays a significant role in defining the CFL along which the maximum of K occurs.

Highlighting a key finding, it's essential to note that in the case of turn-to-turn insulation using rectangular insulated wires, the fillet side consistently hosts the maximum K value, distinct from the edgewise side. This finding essentially signifies that the occurrence of PD is steadily rooted in the fillet side. This insight holds profound implications for our approach. That's exactly the reason for exclusively focusing on the field lines tied to the fillet side during the electrostatic simulations, as depicted in Fig. 5. This newfound understanding underscores the paramount role of the fillet side, with specific emphasis on the *FR*, in determining PDIV for rectangular wires. This should not be underestimated. It is worthwhile to mention that the insulated wire's length and width outside the fillet radius do not affect the PDIV. These dimensions have no impact on the electric field intensity in the air gap between adjacent insulated wires. PDIV is directly influenced by crucial factors such as insulation thickness, permittivity, and fillet radius, determining the electric field distribution within the gap. Thus, whether we aim to design PD-free insulation for electrical machines or produce rectangular insulated wires, such as edgewise insulated wires, the fillet area demands concentrated attention. This entails not only optimizing the *FR* but also meticulously determining the insulation thickness at the fillet side, with a priority surpassing that of the edgewise side. By following the procedure outlined earlier, Fig. 8 illustrates the derived K values from 16 distinct PDIV percentiles (ranging from 0.1% to 99.9% probability), spanning from 5.11 to 6.24.

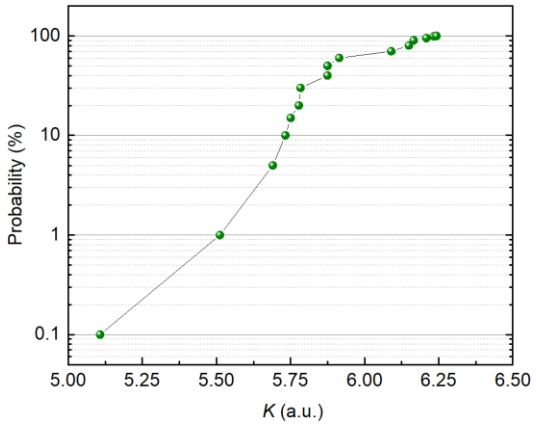

Fig 8. Obtained K from different percentiles of measured PDIV.

D. PDIV Probabilistic Predictive Model

It has been observed in [9] that the fitting parameter K remains unaffected by the wire's geometry and insulating material properties within a specific insulation type (e.g., turn-to-turn using either round or flat conductors). As a result, the K values obtained in Fig. 8 can be fed to the FEM-based model for the prediction of PDIV with the desired probability, specifically for turn-to-turn insulation composed of rectangular wires featuring varying fillet radii under predetermined environmental conditions.

Considering this perspective, the iterative algorithm introduced in [10]-[13] is expanded to predict PDIV across various probabilities, taking into account the *FR* as a variable. The following steps elucidate the outlined procedure:
1) Select a value for K that aligns with the desired probability (see Fig. 8).
2) Choose the preferred *FR* and perform a simulation of the electric field distribution using a unit voltage (1 V) to generate the database (see Fig. 5).
3) Begin with an arbitrary initial PDIV value lower than the actual PDIV (e.g., 50 V).
4) Enhance the electric field intensity along each field line within the imported database in step 2 through linearity, as described in (4).
5) Based on the electric field strength computed in step 4, determine α_{eff} for each field line using the BOLSIG+ software [23], [24].

6) Consider the chosen probabilistic K value from step 1, the computed FLLs from step 2, and the derived α_{eff} from step 5 for all the field line numbers, n_{FL}. Ascertain if the condition (2) holds true for at least one electric field line. If (2) is not met, elevate the applied voltage (e.g., by 0.5 V) and return to step 4.
7) The conclusion point for the iterative process emerges when the condition specified in (2) is guaranteed for at least one field line. Upon achieving this condition, halt the iteration and record the applied voltage as the anticipated PDIV with the desired probability for the chosen *FR*. For each *FR*, this process is repeated for all the 16 K values illustrated in Fig. 8 to calculate the 16 PDIV percentiles (ranging from 0.1% to 99.9% probability). Fig. 9 presents a flowchart that briefly summarizes the iterative approach employed to develop the PDIV probabilistic predictive model.

Finally, for each *FR*, a linearized Weibull probability distribution as (5) is fitted to the predicted PDIV percentiles:

$$\ln\left(-\ln\left(1-F(PDIV_i)\right)\right)=\beta\cdot\ln(PDIV_i)-\beta\cdot\ln(\alpha) \quad (5)$$

where $PDIV_i$ represents one of the PDIV percentiles obtained through the probabilistic predictive model, and $F(PDIV_i)$ stands for the cumulative probability corresponding to $PDIV_i$. This approach allows us to determine both the scale parameter α (representing the 63.2% percentile of PDIV) and the shape/slope parameter β (where larger β values indicate lower PDIV dispersion levels) for the Weibull distribution associated with PDIV concerning a specific *FR*. The detailed method for estimation of α and β from the linearized Weibull distribution (5) can be found in [5].

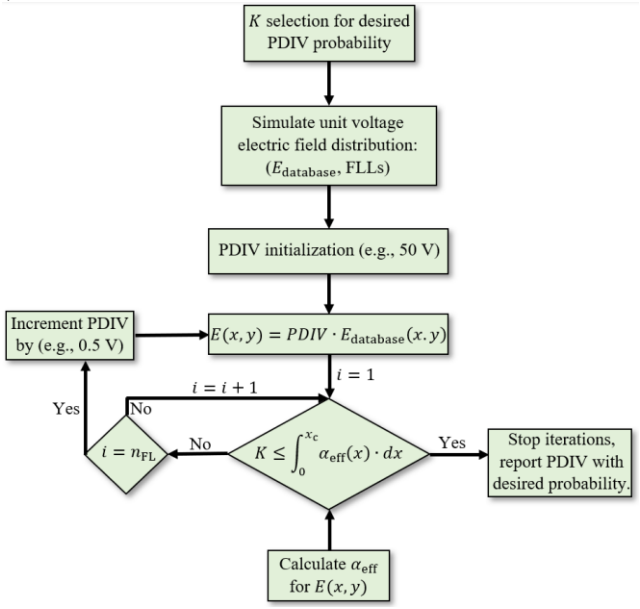

Fig. 9. Flowchart illustrating the iterative approach for the PDIV probabilistic predictive model.

IV. Results and Discussions

A. PDIV

Table II presents the predictions for the reference *FR* (R_{fillet} = 0.4 mm). It outlines both the measured and modelled B10, α, and β of the PDIV peak, as determined through the method detailed in section III and (5). Table II clearly illustrates the close alignment between predicted values and test data, affirming the model's effective ability to forecast measurement dispersion by deriving β of PDIV. This extends the model's applicability beyond the validated scope discussed in [10]-[13].

TABLE II
Modelled vs Measured Weibull Parameters

Parameter	Measured	Modelled	Error (%)
B10 (V)	937	923	-1.52
α (V)	965	954	-1.15
β (a.u.)	74.4	68.1	-9.25

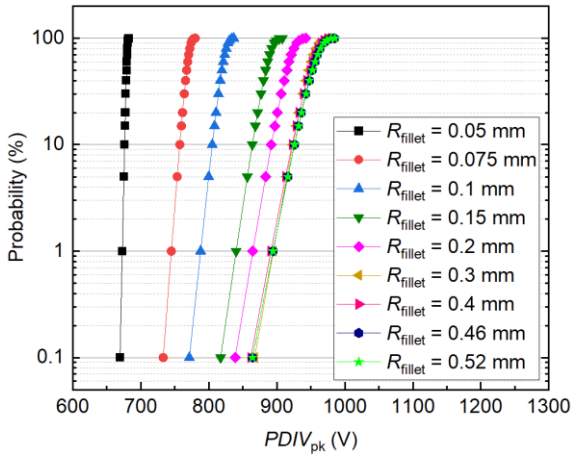

Fig 10. Estimated percentiles of PDIV peak for different fillet radii.

Therefore, as illustrated in Fig. 10, it is possible to predict PDIV with various probabilities corresponding to the 2-parameter Weibull distribution using the experimentally derived K values presented in Fig. 8 and the PDIV prediction algorithm detailed in Section III. Fig. 10 indicates the impact of *FR* on the PDIV of turn-to-turn insulation in rectangular insulated wires. The graph depicts both the PDIV value and its probability of occurrence. It is evident that increasing the *FR* leads to an initial increase in PDIV up to a certain point, R_{fillet} = 0.3 mm. Beyond this saturation point (i.e., R_{fillet} = 0.3 mm), the change in PDIV becomes negligible. Furthermore, Fig. 10 demonstrates that as the *FR* decreases, the slope of the Weibull chart increases, indicating a reduction in PDIV dispersion. The PDIV dispersion follows an almost similar pattern as the PDIV magnitude with respect to the *FR*, reaching a threshold level where the slope of the Weibull chart or the PDIV dispersion stabilizes and shows minimal changes.

To provide a quantitative view and enhance clarity, Fig. 11 presents the predicted PDIV using two different K values, along with the shape/slope parameter of the 2-parameter Weibull distribution (i.e., β), as a function of *FR*. One K value ($K_{\text{mean}} = 5.95$) is derived from the mean of the measured PDIV at R_{fillet} = 0.4 mm, while another K value ($K_{\text{B10}} = 5.73$) is obtained from the B10 of PDIV after fitting the measured values for R_{fillet} = 0.4 mm to the 2-parameter Weibull distribution as shown in Fig. 7. This implies that, even though the chosen K values may appear relatively close, they exhibit

notable differences from a probability perspective. Fig. 11 clearly demonstrates that PDIV increases by approximately 28% as the *FR* grows from R_{fillet} = 0.05 mm to R_{fillet} = 0.3 mm, reaching a saturation point at R_{fillet} = 0.3 mm.

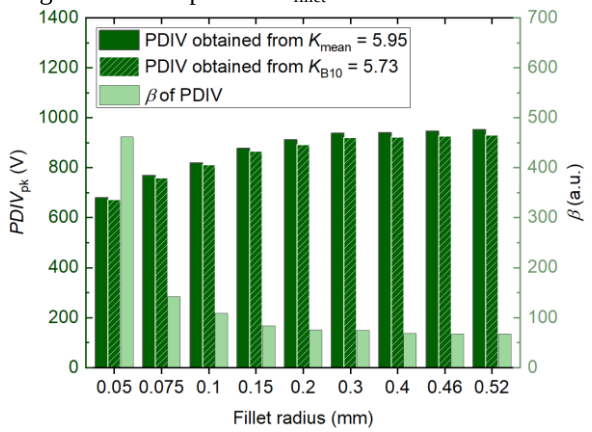

Fig 11. Estimated mean, B10 and β of PDIV peak as a function of *FR*.

This implies that by increasing the *FR* from 0.05 mm to 0.3 mm taking into account the PD-free design for inverter-fed motors, the DC bus voltage can be raised by 28%, ensuring less risk for PD inception between the turn-to-turn insulation. Regarding PDIV dispersion, Fig. 11 reveals that beyond R_{fillet} = 0.2 mm, the change in PDIV dispersion becomes negligible. Specifically, when using fillet radii less than R_{fillet} = 0.075 mm, the β of PDIV exhibited a notable increase, signifying a considerable reduction in PDIV dispersion. For instance, at R_{fillet} = 0.05 mm, the β of PDIV is nearly 6 times higher than at R_{fillet} = 0.2 mm. The increase in β of PDIV at a 0.05 mm fillet radius occurs because this critical radius reduces the air gap between the insulated wires, accommodating fewer field lines. This reduction in field lines decreases the dispersion of FLLs and their corresponding electric fields. Consequently, the probability of PD inception increases when the applied voltage and, subsequently, the electric field in the air gap reach a certain level. This leads to a lower dispersion level of PDIV at smaller fillet radii, as indicated by a larger β of PDIV.

B. CFLL

Fig. 12 illustrates the relationship between CFLL and the *FR*, normalized to the reference value of R_{fillet} = 0.4 mm. Overall, an increase in the *FR* results in a shortening CFLL. For example, in the case of K_{B10}, CFLL decreases by nearly 2.5 times from R_{fillet} = 0.05 mm to 0.52 mm. However, the sensitivity of CFLL to *FR* varies depending on the range of fillet radii. For instance, within the range of R_{fillet} = 0.075 mm to 0.3 mm, CFLL remains constant, and the same applies to the obtained CFLL from K_{mean} within the range of R_{fillet} = 0.4 mm to 0.52 mm. Comparing the obtained CFLL from K_{mean} and K_{B10}, they are generally similar except for the cases of the smallest and largest fillet radii. As the fillet radius decreases, the air gap between adjacent wires shrinks, necessitating an increase in CFLL to boost ionization events per unit length. This establishes conditions essential for PD initiation along the field line. It is important to note that a longer CFLL associated with the shortest *FR* implies a greater potential for harmful effects or damage due to PD activity.

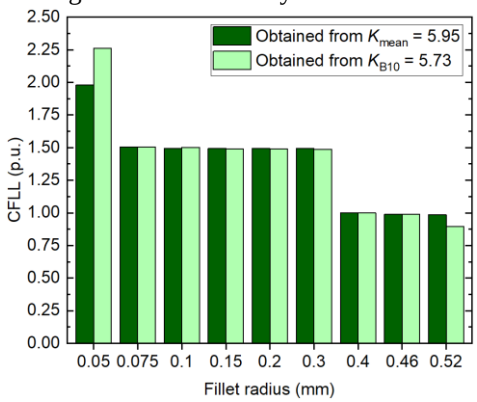

Fig. 12. CFLL vs *FR* obtained from K_{mean} and K_{B10}, normalized to CFLL of R_{fillet} = 0.4 mm.

This is because a longer CFLL results in a single electron, starting an avalanche, travelling a longer path, and acquiring more kinetic energy. Consequently, there is a higher likelihood of having hot electrons with energies exceeding the bond energies of the insulation (typically 3-4 eV for Carbon-Carbon and Carbon-Hydrogen bonds), leading to an increased risk of Dissociative Electron Attachment (DEA) and causing more damage on the insulation surface due to PD activity [11]-[13]. To emphasize, even a slight reduction in the *FR*, for example, from 0.4 mm to 0.3 mm, results in a 1.5 times longer CFLL. This implies that while both fillet radii have almost the same PDIV as shown in Fig. 11, PD activity at R_{fillet} = 0.3 mm leads to higher damage, thus a longer lifetime is predicted at the same overvoltage with respect to PDIV for R_{fillet} = 0.4 mm, representing an optimum *FR*.

Therefore, when the edge of the rectangular wire is sharp enough (e.g., R_{fillet} = 0.05 mm), there are two significant disadvantages. First, it results in a lower PDIV (see Fig. 11). Second, it increases the destructive potential of PD. This means that at the same overvoltage with respect to PDIV, comparing R_{fillet} = 0.05 mm and R_{fillet} = 0.52 mm, more damage would be plausible when the edge of the rectangular wire is less rounded (i.e., R_{fillet} = 0.05 mm). These considerations are crucial in the manufacturing of rectangular insulated wires, especially when moderate PD activity is anticipated, such as in the case of corona-resistant insulation. It will help prevent undesirably short lifetimes of the wires and ensure their reliable performance.

C. PD Inception Field

Fig. 13 depicts the variations of the PD inception field (E_{inc}) plotted as a function of the *FR*, which has been normalized to the reference value of R_{fillet} = 0.4 mm (2.8 kV/mm). The PD inception field, assigned along the CFL under PDIV conditions, may differ from the maximum electric field between two insulated wires. The highest electric field occurs across the shortest field line, which may not coincide with the CFL. It is

essential for the field line to be sufficiently long and possess a significant electric field for the initial electron to generate the required ionization events per unit length, ensuring conditions for the avalanche to reach its critical size.

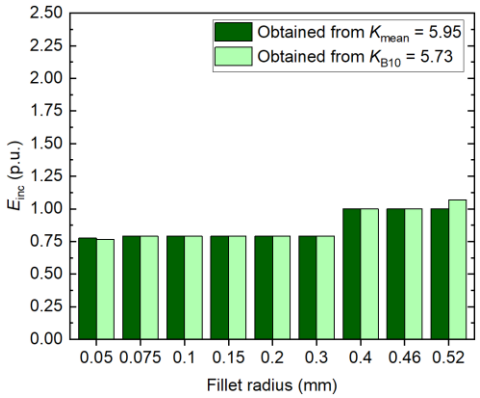

Fig. 13. E_{inc} vs FR obtained from K_{mean} and K_{B10}, normalized to E_{inc} of R_{fillet} = 0.4 mm.

The graph illustrates that E_{inc} experiences a reduction of 1.3 times when transitioning from R_{fillet} = 0.4 mm to R_{fillet} = 0.3 mm, emphasizing the superiority of the former to the latter. However, within a broader range of FR variations, from R_{fillet} = 0.3 mm to R_{fillet} = 0.05 mm (where PDIV reduces as shown in Fig. 11), E_{inc} remains relatively steady. Moreover, from R_{fillet} = 0.4 mm to R_{fillet} = 0.52 mm, E_{inc} exhibits almost constant behaviour, similar to PDIV (see Fig. 11). Furthermore, it becomes evident that, except for the largest FR (R_{fillet} = 0.52 mm), both K_{mean} and K_{B10} deliver the same E_{inc} values.

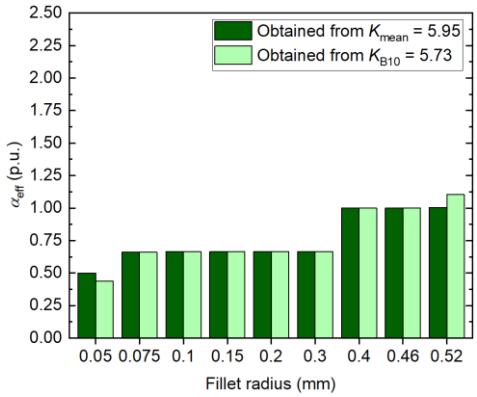

Fig. 14. α_{eff} vs FR obtained from K_{mean} and K_{B10}, normalized to α_{eff} of R_{fillet} = 0.4 mm.

D. Air Effective Ionization Coefficient

Fig. 14 displays the variations of α_{eff} across the CFL as a function of the FR, which has been normalized to the value obtained at R_{fillet} = 0.4 mm. In general, a decrease in the FR leads to a lower α_{eff}. This decrease can be attributed to either a lower PD inception field (E_{inc}) or a longer CFL at a constant avalanche size. For instance, with K_{B10}, α_{eff} decreases by nearly 2.5 times when moving from R_{fillet} = 0.52 mm to 0.05 mm, which is in contrast to CFLL. However, similar to CFLL, the sensitivity of α_{eff} to the FR varies depending on the range of fillet radii. For instance, α_{eff} remains constant within the range of R_{fillet} = 0.075 mm to 0.3 mm, and the same applies to the obtained α_{eff} from K_{mean} within the range of R_{fillet} = 0.4 mm to 0.52 mm. Comparing the obtained α_{eff} from K_{mean} and K_{B10}, they are generally similar except for the cases of the smallest and largest fillet radii. When α_{eff} is low, it indicates that air molecules are less likely to undergo ionization. However, this low α_{eff} does not result in a higher PDIV when the FR is the smallest (see Fig. 11). This suggests that, at a constant avalanche size, the impact of a longer CFL in delivering a lower PDIV outweighs the effect of a lower α_{eff} when the FR is smaller. In fact, for ionization to occur, air molecules must be exposed to a certain amount of energy, and a longer CFL corresponding to a lower FR can provide this necessary energy, resulting in a lower PDIV.

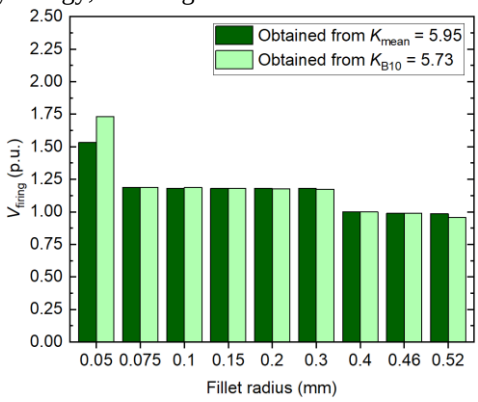

Fig. 15. V_{firing} vs FR obtained from K_{mean} and K_{B10}, normalized to V_{firing} of R_{fillet} = 0.4 mm.

E. Firing Voltage

Another parameter linked to streamer inception is the firing voltage, V_{firing}, which is determined by multiplying E_{inc} with CFLL, as reported in Figs. 13 and 12, respectively. Fig. 15 illustrates the variations of V_{firing} concerning the FR, which has been normalized to the value obtained at R_{fillet} = 0.4 mm. The graph clearly demonstrates that V_{firing} reaches its peak when the FR is at its smallest. For instance, at R_{fillet} = 0.05 mm, V_{firing} is approximately 1.81 times higher than at R_{fillet} = 0.52 mm. At the smallest FR, both E_{inc} and CFLL reach their lowest and longest values, respectively. Consequently, the impact of CFLL on V_{firing} outweighs the effect of E_{inc}, leading to the highest V_{firing} at the smallest FR.

It is important to highlight that a clear linear relationship exists between the firing voltage and PD charge amplitude, as demonstrated in [25]. Furthermore, there is a well-established linear relationship between the PD charge amplitude and the harmfulness associated with PD activity, as indicated in [26]-[28]. Consequently, it logically follows that there is a linear relationship between the firing voltage and the harmfulness associated with PD activity. In summary, Fig. 15 provides compelling evidence that as the FR decreases, the firing voltage increases, indicating a higher level of damage for smaller fillet radii. This observation is consistent with the findings obtained from CFLL calculations presented in Fig. 12, where higher

damage is linked to the longest CFL at the smallest *FR*. Consequently, the destructive potential of PD is greater at a smaller *FR* due to both the longer CFL and higher V_{firing}. A noteworthy observation emerges from comparing R_{fillet} values of 0.3 mm and 0.4 mm. Even a slight 0.1 mm increment in *FR* leads to nearly a 15% decrease in firing voltage, indicating reduced damage and an extended lifetime under the same PDIV overvoltage for R_{fillet} = 0.4 mm. This aligns with findings from CFLL and E_{inc} analyses, thus introducing R_{fillet} = 0.4 mm as the optimal fillet radius. It is important to note that selecting different *K* values from both K_{mean} and K_{B10}, as illustrated in various values in Fig. 8, does not result in a different optimal fillet radius from the identified value of 0.4 mm.

V. Conclusion

This contribution presents a probabilistic PDIV prediction model rooted in SCSIC, providing valuable support for insulation designers in electrical machines and coil winding wire manufacturers. The model aids in the optimal selection of *FR* for rectangular insulated wires, achieving maximum PDIV while minimizing damage, thus enhancing insulation reliability. The model emphasises the decisive influence of the *FR* on the PDIV since the fitting parameter *K* consistently peaks at the fillet site. It demonstrates that PDIV increases with larger fillet radii, reaching a saturation point where further increases do not affect PDIV value. Moreover, the probabilistic PDIV model shows that reducing *FR* leads to lower PDIV and reduced dispersion. Associated with PD activity, SCSIC-derived SIPs like CFLL and V_{firing} also decrease with increased *FR*, even post-PDIV saturation. This guarantees reduced damage and increased lifetime. The approach developed in this study simplifies the selection of the optimal wire geometry, specifically *FR*. It eliminates the need for extensive, time-consuming, and costly insulation qualification tests, including accelerated life tests.

References

[1] C. Li, Y. Yang, G. Xu, Y. Zhou, M. Jia, S. Zhong, Y. Gao, C. Park, Q. Liu, Y. Wang, and S. Akram, "Insulating materials for realising carbon neutrality: Opportunities, remaining issues and challenges," *High Voltage*, vol. 7, no. 4, pp. 610-632, 2022.

[2] T. Wakimoto, H. Kojima, and N. Hayakawa, "Measurement and evaluation of partial discharge inception voltage for enamelled rectangular wires under AC voltage," *IEEE Trans. Dielectr. Electr. Insul.*, vol. 23, no. 6, pp. 3566-3574, Dec. 2016.

[3] T. Okada, H. Matsumori, T. Kosaka, and N. Matsui, "Hybrid excitation flux switching motor with permanent magnet placed at middle of field coil slots and high filling factor windings," *CES Trans. Electr. Mach. Syst.*, vol. 3, no. 3, pp. 248-258, Sept. 2019.

[4] IEC Std. 60034-18-41, "Rotating electrical machines - part 18-41: partial discharge free electrical insulation systems (Type I) used in rotating electrical machines fed from voltage converters - qualification and quality control tests," 2019.

[5] P. Mancinelli, S. Stagnitta and A. Cavallini, "Qualification of hairpin motors insulation for automotive applications," *IEEE Trans. Ind. Appl.*, vol. 53, no. 3, pp. 3110-3118, May-June 2017.

[6] A. Cavallini, D. Fabiani, and G. C. Montanari, "Power electronics and electrical insulation systems - part 2: life modeling for insulation design," *IEEE Electr. Insul. Mag.*, vol. 26, no. 4, pp. 33-39, Jul-Aug. 2010.

[7] H. Naderiallaf, M. Degano, C. Gerada, "Assessment of edgewise insulated wire bend radius impact on dielectric properties of turn-to-turn insulation through thermal ageing," *IEEE Trans. Electr. Insul.*, pp. 1-10, Aug. 2023.

[8] L. Lusuardi, A. Cavallini, M. G. de la Calle, J. M. Martínez-Tarifa, and G. Robles, "Insulation design of low voltage electrical motors fed by PWM inverters," *IEEE Electr. Insul. Mag.*, vol. 35, no. 3, pp. 7-15, May-Jun. 2019.

[9] J. Gao, A. Rumi, Y. He and A. Cavallini, "Towards a holistic approach to inverter-fed machine design: FEM-based PDIV prediction of complete windings," *IEEE Transactions on Dielectrics and Electrical Insulation*, June 2023.

[10] H. Naderiallaf, M. Degano, C. Gerada, "PDIV modeling for rectangular wire turn-to-turn insulation of inverter-fed motors through thermal ageing," *IEEE Trans. Electr. Insul.*, pp. 1-10, Aug. 2023.

[11] H. Naderiallaf, Y. Ji, P. Giangrande, and M. Galea, "Temperature impact on PDIV for turn-to-turn insulation of inverter-fed motors: from ground level to cruising altitude," *IEEE Trans. Electr. Insul.*, pp. 1-10, Sep. 2023.

[12] H. Naderiallaf, Y. Ji, P. Giangrande, and M. Galea, "Air pressure impact on the avalanche size for turn-to-turn insulation of inverter-fed motors," *IEEE Trans. Electr. Insul.*, pp. 1-10, Oct. 2023.

[13] H. Naderiallaf, Y. Ji, P. Giangrande, and M. Galea, "Modeling humidity impact on PDIV for turn-to-turn insulation of inverter-fed motors at different temperatures," *IEEE Trans. Electr. Insul.*, pp. 1-10, Nov. 2023.

[14] G. C. Montanari and P. Seri, "About the definition of PDIV and RPDIV in designing insulation systems for rotating machines controlled by inverters," in *2018 IEEE Electrical Insulation Conference (EIC)*, 2018, pp. 554-557.

[15] C. Abadie, "On-line non-intrusive partial discharge detection in aeronautical systems," Ph.D. dissertation, University of Toulouse, 2017.

[16] H. Naderiallaf, P. Giangrande, and M. Galea, "Characterization of PDIV, PDEV, and RPDIV in insulated wires under unipolar repetitive square wave excitations for inverter-fed motors," *IEEE Access*, vol. 11, pp. 51047-51063, 2023.

[17] M. Goldman, A. Goldman, and J. Gatellet, "Physical and chemical aspects of partial discharges and their effects on materials," in *1993 International Conference on Partial Discharge*, 1993, pp. 11-14.

[18] H. Raether, "Electron avalanches and breakdown in gases," *Butterworth and Co. Publishers Ltd.*, 1964.

[19] W. O. Schumann, "Über das Minimum der Durchbruchfeldstärke bei Kugelelektroden," *Arch. Elektrotech. (Berl.)*, vol. 12, pp. 593-608, 1923 (in German).

[20] N. H. Malik, "Streamer breakdown criterion for compressed gases," *IEEE Trans. Electr. Insul.*, vol. EI-16, no. 5, pp. 463-467, Oct. 1981.

[21] H. Naderiallaf, P. Giangrande and M. Galea, "Investigating the effect of space charge accumulation on partial discharge activity for new and thermally aged glass fibre insulated wire," in *2023 INSUCON - 14th International Electrical Insulation Conference (INSUCON)*, Birmingham, United Kingdom, 2023, pp. 39-43.

[22] H. Naderiallaf, P. Giangrande and M. Galea, "Experimental considerations on the possible impact of space charge accumulation on partial discharges activity for wire insulations," in *2022 IEEE 4th International Conference on Dielectrics (ICD)*, Palermo, Italy, 2022, pp. 82-85.

[23] G. J. M. Hagelaar and L. C. Pitchford, "Solving the Boltzmann equation to obtain electron transport coefficients and rate coefficients for fluid models," *Plasma Sources Sci. Technol.*, vol. 14, no. 4, pp. 722-733, 2005.

[24] "BOLSIG+ | Electron Boltzmann equation solver." [Online]. Available: http://www.bolsig.laplace.univ-tlse.fr/. [Accessed: Mar. 20, 2023].

[25] P. Seri, H. Naderiallaf, and G. C. Montanari, "Modelling of supply voltage frequency effect on partial discharge repetition rate and charge amplitude from AC to DC at room temperature," *IEEE Trans. Dielec. Electr. Insul.*, vol. 27, no. 3, pp. 764-772, June 2020.

[26] H. Naderiallaf, P. Seri and G. C. Montanari, "Effect of voltage slew rate on partial discharge phenomenology during voltage transient in HVDC insulation: the case of polymeric cables," *IEEE Trans. Electr. Insul.*, vol. 29, no. 1, pp. 215-222, Feb. 2022.

[27] H. Naderiallaf, R. Ghosh, P. Seri and G. C. Montanari, "HVDC insulation systems: effect of voltage polarity inversion slew rate on partial discharge phenomenology and harmfulness," in *22nd International Symposium on High Voltage Engineering (ISH 2021)*, Hybrid Conference, Xi'an, China, 2021, pp. 7-12.

[28] H. Naderiallaf, P. Seri, and G. C. Montanari, "DC cables: effect of voltage transient slew rate on partial discharge phenomenology and harmfulness" In *Jicable*, vol. 21, pp. 1-4. 2021.